Chinese Chemical Letters 34 (2023) 108142

Contents lists available at ScienceDirect

Chinese Chemical Letters

journal homepage: www.elsevier.com/locate/cclet

Ordered mesoporous carbon fiber bundles with high-density and accessible Fe-N$_X$ active sites as efficient ORR catalysts for Zn-air batteries

Fengxian Zhang[1], Xupo Liu[1], Ye Chen, Miao Tian, Tianfang Yang, Jing Zhang, Shuyan Gao*

School of Materials Science and Engineering, Henan Normal University, Xinxiang 453007, China

ARTICLE INFO

Article history:
Received 25 November 2022
Revised 21 December 2022
Accepted 10 January 2023
Available online 13 January 2023

Keywords:
Oxygen reduction reaction
Ordered mesoporous carbon
High-density Fe-N$_x$ sites
Accessibility
Zn-air battery

ABSTRACT

Fe-N$_X$/C electrocatalysts have aroused extensive interest in accelerating sluggish oxygen reduction reaction (ORR) kinetics as potential alternatives to platinum catalysts in rechargeable Zn-air batteries (ZABs). However, the low density and poor accessibility of Fe-N$_X$ sites have severely restricted the electrocatalytic performance of Fe-N$_X$/C. Herein, Fe, N co-doped ordered mesoporous carbon fiber bundles are prepared through a ligand-assisted strategy with nitrogen-rich 1,10-phenanthroline as space isolation agent. 1,10-Phenanthroline reveals a six-membered heterocyclic structure containing abundant nitrogen species to tightly coordinate with Fe ions, which is conducive to achieving high-density Fe-N$_X$ sites. Meanwhile, the adoption of SBA-15 as hard-templates enables the catalysts with highly ordered channels and large specific surface areas, improving the accessibility of Fe-N$_X$ sites. The optimal catalyst (PDA-Fe-900) demonstrates a positive half-wave potential of 0.84 V (*vs.* RHE) in alkaline solution, outperforming the commercial Pt/C (0.83 V). In addition, PDA-Fe-900 delivers comparable ORR performance to commercial Pt/C in acidic electrolyte. Impressively, when PDA-Fe-900 is employed as an air cathode, it achieves large power densities of 163.0 mW/cm^2 in liquid-state ZAB and 116.6 mW/cm^2 in the flexible solid-state ZAB. This work provides an efficient ligand-assisted pathway for fabricating catalysts with dense and accessible Fe-N$_X$ sites as high-performance ORR electrocatalysts for ZABs.

With the rapid consumption of fossil fuels and the increasingly serious environmental problems, developing clean and efficient electrochemical energy conversion and storage technology is crucial for promoting the green, low-carbon, and sustainable society [1–5]. As a promising energy storage system, rechargeable Zn-air batteries (ZABs) have been widely explored owing to their high theoretical energy density (1084 Wh/kg), low-cost and environment friendliness [6–9]. However, the sluggish kinetics and high overpotentials of the oxygen reduction reaction (ORR) at the air cathode significantly hinder the commercial application of ZABs [10–12]. At present, precious metal-based electrocatalysts such as platinum (Pt) and its complex exhibit superior ORR catalytic activity, but their scarcity, prohibitive cost, and poor stability have significantly restricted their scalable application [13]. To overcome these barriers, the development of cost-effective, highly efficient and stable non-precious metal-based ORR electrocatalysts is of great importance for the practical application of rechargeable ZABs [14,15].

In recent years, transition metal and nitrogen co-doped carbon (M-N$_X$/C) materials have received tremendous progress as cathode ORR electrocatalysts for ZABs. Among them, Fe-N$_X$/C catalysts have been taken as one of the most promising alternatives to precious metal-based catalysts for ORR due to their excellent electrocatalytic activity and abundant resources [16–19]. Both experimental and theoretical studies have shown that Fe-N$_X$ configuration embedded in the carbon matrix is the mainly active sites for improving ORR catalytic activity because it can promote the adsorption of O$_2$ and destroy the O–O bond [20–23]. Therefore, anchoring Fe atoms into carbon matrix in the form of Fe-N$_X$ sites is an effective way to improve the ORR performance. Since Fe atoms tend to agglomerate to form inactive nanoparticles during the high-temperature treatment, most reported Fe-N$_X$/C catalysts possess low-density Fe-N$_X$ active sites, resulting in insufficient ORR catalytic activity [24–26]. The key route to improve the density of Fe-N$_X$ sites is to realize the in-situ anchoring of Fe ions in the process of synthesis [27]. Generally, nitrogen-rich small molecules are able to anchor Fe ions and form the precursor analogous to Fe-N$_X$ species, resulting in

---

* Corresponding author.
E-mail address: shuyangao@htu.cn (S. Gao).

[1] These authors contributed equally to this work.

https://doi.org/10.1016/j.cclet.2023.108142
1001-8417/© 2023 Published by Elsevier B.V. on behalf of Chinese Chemical Society and Institute of Materia Medica, Chinese Academy of Medical Sciences.

well-dispersed Fe atoms in the precursors. Therefore, rational selection of nitrogen-containing precursors is an effective solution to prevent the aggregation of metal Fe species during pyrolysis to ensure the formation of dense Fe-N$_X$ sites [28]. Besides, not all of the Fe-N$_X$ sites can participate in ORR process because most of catalysts are of relatively low surface area and/or disordered channels, which limit the accessibility of Fe-N$_X$ sites and mass transfer [29]. Some reports have demonstrated that the ordered mesoporous structure can supply high surface area, regular and ordered mass transfer channels, and thus effectively increase the exposure of Fe-N$_X$ sites [30–32]. Therefore, optimizing the mesopore structure of catalyst is of great significance to improve the accessibility of Fe-N$_X$ active sites in ORR [33–35]. Based on the above analysis, developing a feasible strategy to construct high-density and accessible Fe-N$_X$ configurations embedded in carbon matrix is desired, but remains a major challenge.

Herein, the dense and accessible Fe-N$_X$ sites decorated ordered mesoporous carbon fiber bundles were prepared through a ligand-assisted strategy using SBA-15 as hard-templates and nitrogen-rich 1,10-phenolline (Phen) as space isolation agent. Phen, as a small molecule precursor, has abundant pyridine nitrogen configuration and is easy to form stable complexes with Fe^{2+}, which is conducive to the formation of high-density Fe-N$_X$ sites during pyrolysis. The ordered mesoporous architecture resulting from SBA-15 hard-templates enables the efficient exposure of Fe-N$_X$ sites and improved mass transfer, as demonstrated in the case of the optimal catalyst PDA-Fe-900. The abundant mesoporous structure with pore size of about 5 nm, high surface areas (1115.0 m^2/g), and high-density accessible Fe-N$_X$ sites make PDA-Fe-900 has excellent ORR activity and stability in both alkaline and acidic media, comparable to that of commercial Pt/C catalyst. The liquid-state ZAB based on catalyst PDA-Fe-900 shows superior performance with a high-power density (163.0 mW/cm^2), good long-term cycle stability (over 160 h), and excellent specific capacity (802.1 mAh/g). Moreover, the assembled flexible solid-state ZAB demonstrates a large power density of 116.6 mW/cm^2 and excellent cycle stability at various bent states (0∼180°), providing a feasible avenue for flexible electronic device applications. These experimental results reveal the significance of optimizing the density and accessibility of Fe-N$_X$ active sites for catalysts, providing a feasible route for the synthesis of non-precious metals ORR catalysts for ZABs.

2,6-Diaminopyridine (DAP, $C_5H_7N_3$), 1,10-phenanthroline (Phen, $C_{12}H_8N_2$), ferrous sulfate ($FeSO_4 \cdot 7H_2O$), potassium hydroxide (KOH) and zinc acetate ($Zn(OAc)_2$) were obtained from Shanghai Aladdin Biochemical Technology Co., Ltd. SBA-15 was purchased from Jiangsu XFNANO material technology Co., Ltd. and zinc plate was from Qinghe Tengfeng metal material Co., Ltd. Hydrofluoric acid (HF) and sulphuric acid (H_2SO_4) were supplied from Shandong Yantai Shuangshuang Chemical Co., Ltd. Nafion (5 wt%), commercial Pt/C (20 wt%) and carbon fiber paper were supplied from Shanghai Hesen Electric Co., Ltd. Electrode composite matrix was purchased from Changsha Spring Co., Ltd. All chemical reagents were employed directly without further purification.

A ligand-assisted strategy was used to synthesize the catalysts. Typically, 0.27 g Phen and 0.16 g $FeSO_4 \cdot 7H_2O$ were dispersed in 25 mL mixed solution of ethanol and deionized water (v:v=1:1) under ultrasonication for 10 min, resulting in the formation of red Fe-Phen complex. Meanwhile, 1.5 g DAP and 0.5 g SBA-15 were dissolved in the above solution and stirred for 1 h at 25 °C. Then, the brown power was obtained after drying and grinding in mortar. The precursor was heated to several different temperatures (700, 800, 900 and 1000 °C) at a heating rate of 5 °C/min. The temperature was maintained for 2 h under the condition of N_2 flow (the heating platform was maintained at 300 °C for 1 h). The product was soaked in 20 wt% HF aqueous solution at 25 °C for 12 h. Finally, after being washed with deionized water until neutral and dried at 80 °C in the oven for 6 h, the ultimate product of PDA-Fe-T was obtained, where *T* stands for pyrolysis temperature ($T = 700$, 800, 900 or 1000 °C). For comparison, the synthetic procedure of PDA-900, DA-Fe-900, PA-Fe-900 and PD-Fe-900 are similar to PDA-Fe-900 without adding $Fe_2SO_4 \cdot 7H_2O$, Phen, DAP and SBA-15, respectively.

Microstructure and morphology of the catalysts were characterized by the scanning electron microscopic (SEM) on a SUPRA40 and transmission electron microscopy (TEM) using TECNAI G2 F30. The crystal phases of samples were identified by powder X-ray diffraction (XRD) patterns employing PANalytical B.V. X' Pert3 Powder apparatus with Cu Kα radiation ($\lambda = 0.154$ nm). Raman spectra were measured directly on LabRAM HR Evolution with 532 nm excitation laser to character the defects degree of catalysts. The element compositions were recorded through X-ray photoelectron spectroscopy (XPS) on ESCALAB250Xi equipment with monochromatic Al Kα. The pore size distribution and Brunauer-Emmett-Teller (BET) surface area of samples were analyzed by N_2 adsorption-desorption isotherms performed to on the Quantachrome Autosorb Station iQ2 instrument. The content of Fe was quantified by an ELAN DRC-e inductively coupled plasma mass spectrometer (ICP-MS). The absorbance of Fe-Phen complex was measured with UV–vis spectrophotometer ($\lambda = 400$ nm).

All electrochemical experiments were carried out on an electrochemical workstation (CHI 660E) with a three-electrode system at room temperature. 1 cm^2 Pt foil, saturated calomel electrode (SCE) (or Hg/HgO electrode), and catalyst-coated glassy carbon electrode (GCE, $d = 3$ mm or 5.61 mm) as the counter electrode, reference electrode and working electrode, respectively. All the potentials in this study have been converted to the reversible hydrogen electrode (RHE) scale. To prepare catalyst ink, 1 mg of the as-prepared sample was ultrasonically dispersed in 10 µL Nafion solution (5 wt%), 95 µL ultrapure water, and 95 µL ethanol. Subsequently, the catalyst ink was dropped onto the surface of GCE to acquire the working electrode (0.5 mg/cm^2). For comparison, the deposition amount of commercial Pt/C catalyst ink was 0.25 mg/cm^2. Cyclic voltammetry (CV) tests were measured in N_2/O_2-saturated 0.1 mol/L KOH or 0.5 mol/L H_2SO_4 media at a scanning rate of 10 mV/s in the potential range of 0.1-1.1 V. Rotating disk electrode (RDE) tests were performed in a N_2/O_2-saturated electrolyte solution at a scan rate of 10 mV/s in the range of 0.1-1.1 V *vs.* RHE at various rotating speed from 400 rpm to 2025 rpm. The electron transfer number (n) can be calculated by the Koutechy-Levich (K-L) equations:

$$\frac{1}{j} = \frac{1}{j_L} + \frac{1}{j_K} = \frac{1}{B\omega^{1/2}} + \frac{1}{j_K} \tag{1}$$

$$B = 0.2nFC_0 D_0^{2/3} \nu^{-1/6} \tag{2}$$

where j, j_L and j_K are the measured current, diffusion-limited current and kinetics current densities, respectively. ω represents the rotation speed (rpm), F stands for the Faraday constant ($F = 96{,}484$), C_0 is the saturated O_2 concentration (pH 13, 1.2×10^{-6} mol/cm^3; pH 0, 1.05×10^{-6} mol/cm^3), D_0 is the diffusion coefficient of O_2 in electrolyte (pH 13, 1.9×10^{-5} cm^2/s; pH 0, 1.4×10^{-5} cm^2/s), and ν is the kinematic viscosity (0.01 cm^2/s).

The rotating speed of the rotating ring-disk electrode (RRDE) measurements was 1600 rpm and the ring potential was set as 1.2-1.5 V to detect the electron transfer number (n) and hydrogen peroxide yield (H_2O_2%) base on the following equations:

$$H_2O_2(\%) = 200\frac{i_R/N}{i_D + i_R/N} \tag{3}$$

$$n = 4\frac{i_D}{i_D + i_R/N} \tag{4}$$

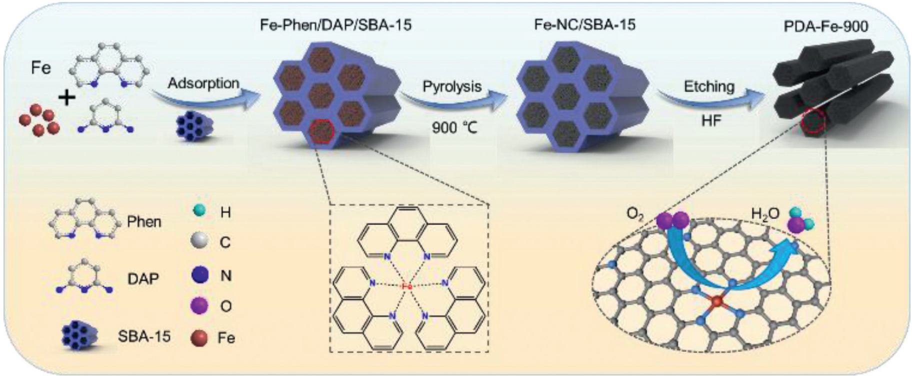

Scheme 1. Schematic synthetic strategy of PDA-Fe-900 catalyst.

Here i_D and i_R are the disk current and ring current, respectively, and N is 0.37.

The long-term cycle stability was performed using scanning potential between 0-1.1 V at scan rate of 50 mV/s for 9000 cycles or 4000 cycles in O_2-satureted 0.1 mol/L KOH or 0.5 mol/L H_2SO_4, respectively. The methanol tolerance test was performed by injecting 1 mL methanol solution into the electrolyte. The electrochemically active surface area (ECSA) of catalysts was evaluated from double-layer capacitance (C_{dl}), which was obtained by measuring double-layer charging from the CVs at different scan rates in non-Faradaic potential range. Electrochemical impedance spectrum (EIS) was measured in the frequency range from 10^5 Hz to 0.01 Hz. For the oxygen evolution reaction (OER), LSV profiles were obtained at a scan rate of 10 mV/s in the potential range of 1.0-2.0 V.

The ZAB experiments were performed by the homemade liquid rechargeable ZAB at room temperature with a CHI660E electrochemical workstation. The catalyst loaded on the gas diffusion layer was employed as the air cathode (loading amount of 1 mg/cm^2), Zn foil (0.2 mm of thickness) as anode and 6.0 mol/L KOH solution containing 0.2 mol/L $Zn(OAc)_2$ as electrolyte. Dispersing 1 mg catalyst to the mixture solution (10 μL Nafion solution (5 wt%), 95 μL ultrapure water, and 95 μL ethanol), the catalyst ink was successfully prepared after sonication. For comparison, Pt/C catalyst was also used as reference air electrode. The polarization curves were recorded by LSV at scan rate of 5 mV/s. Galvanostatic discharge-charge cycling tests were carried out to evaluate the catalyst durability. The discharge and charge periods were set to be 10 min at a given current density of 5 mA/cm^2. For galvanostatic discharge results, the specific capacity and energy density were calculated according to the following equation:

$$\text{Specific capacity} = \frac{\text{current} \times \text{service hours}}{\text{weight of consumed zinc}} \tag{5}$$

The flexible solid-state ZAB was assembled with Zn plate (0.2 mm thickness) and air electrode placed on the two sides of gel electrolyte, and the adhesive tape were used to seal the device. The air cathode was obtained by dropping catalyst ink (1.0 mg catalyst dispersed in 95 μL of ethanol, 95 μL DI water and 10 μL Nafion (5 wt%) solution) onto carbon paper with gas diffusion-layers and nickel foam current collectors (the loading was 1 mg/cm^2). The prepare of solid-state gel electrolyte: 0.03 g methylene bisacrylamide and 190.25 μL acrylic acid were added into 2 mL of 11.25 mol/L KOH and 0.25 mol/L ZnO mixed solution for ultrasonic treatment for 5 min. Then, 30 μL of saturated $K_2S_2O_8$ was added to the above solution and stirred quickly for 10 s. Finally, the prepared gel electrolyte was left at the room temperature for a period of time to allow it to take shape. The galvanostatic charge-discharge curves were tested at a current density of 1 mA/cm^2 with 10 min per cycle.

The preparation of PDA-Fe-900 catalyst has been carried out by employing SBA-15 as templates through a ligand-assisted strategy, as illustrated in Scheme 1. Typically, PDA-Fe-900 is prepared by mixing $FeSO_4 \cdot 7H_2O$ and Phen ligands in a mixed solution of ethanol and water, followed by the adding of DAP and SBA-15. Phen ligands are employed as the main space isolation agents of Fe^{2+} to promote the forming of Fe-N bonds, while DAP is selected as C precursor and simultaneously provide N sites to coordination with additional Fe^{2+}. The formation of Fe-Phen complex is confirmed by UV-visible absorption spectra [36]. Compared with that of Phen ligands, the spectrum of Fe-phen complex solution shows an obvious maximum peak near the wavelength of 510 nm (Fig. S1 in Supporting information). This peak and the red color of the solution indicate that the Fe-Phen complex has been synthesized. Due to the discreteness of Fe-phen complex, the aggregation of metal Fe atoms can be effectively avoided during annealing, which is conducive to the formation of high-density and uniformly distributed Fe-N_X sites. During ethanol evaporation, Fe-Phen complex and DAP are easily dissolved in ethanol and fixed in the pore of SBA-15, forming the framework of ordered mesoporous structure. The ordered mesoporous structure of catalysts is of significance for the accessibility of Fe-N_X sites, mass transfer, and interfacial charge transfer [37–39]. The obtained sample is denoted as Fe-Phen/DAP/SBA-15. After pyrolysis at 900 °C under nitrogen atmosphere and acid leaching, Fe-Phen/DAP/SBA-15 is converted into the ordered mesoporous carbon fiber bundles with dense and accessible Fe-N_X sites (PDA-Fe-900).

Small-angle XRD pattern of PDA-Fe-900 clearly displays a diffraction peak corresponding to the (100) facet of ordered mesoporous carbon frameworks, indicating the generation of long-rang ordered mesoporous structure after removal of SBA-15 templates (Fig. 1a). As shown in the SEM images (Figs. 1b and c), the as-prepared PDA-Fe-900 catalyst exhibits the inverse replicate of the rod-like morphology of SBA-15 templates (Fig. S2 in Supporting information) with a highly ordered mesoporous structure. The TEM image reveals the diameter of the ordered one-dimensional mesoporous carbon fiber in PDA-Fe-900 catalyst as thin as ~5 nm (Fig. 1d), which not only accelerates the transportation of reactants/intermediates but also exposes abundant active sites for electrocatalysis. The HR-TEM was performed to further observe the microstructures of PDA-Fe-900 catalyst. Fig. 1e exhibits the visible fringes with an interplanar spacing of 0.386 nm, which corresponds to the (002) crystal plane of graphite carbon. The partially graphitized nature of carbon framework in PDA-Fe-900 catalyst is beneficial for promoting the conductivity and corrosion resistance of carbon materials. Particularly, no lattice fringes of nanoparticles or nanoclusters are observed from the HR-TEM image of PDA-

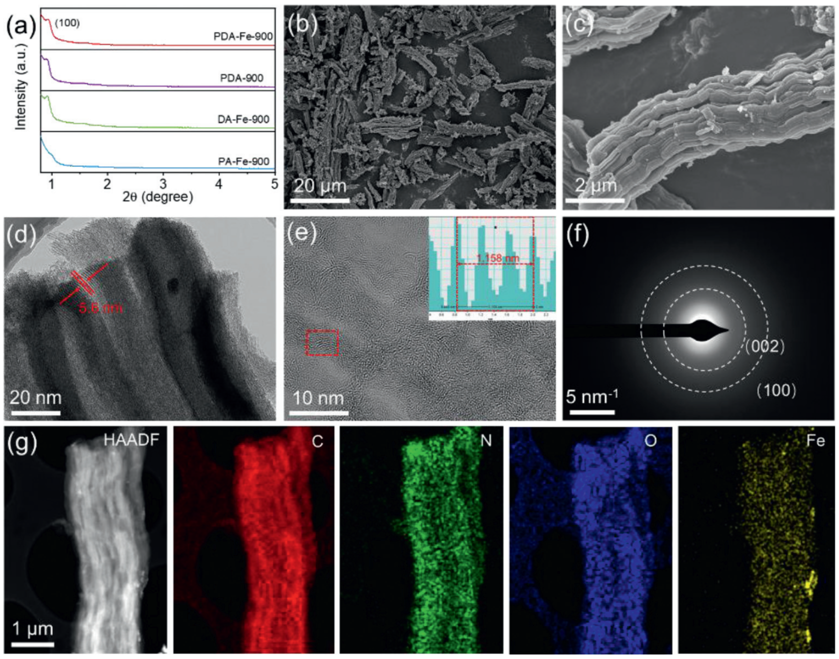

Fig. 1. Structural characterization: (a) Small-angle XRD patterns of PDA-900, PDA-Fe-900, PA-Fe-900 and DA-Fe-900. (b, c) SEM images, (d) TEM image, (e) HR-TEM image, (f) SAED pattern, (g) HAADF-STEM image and the corresponding EDS element mappings of PDA-Fe-900.

Fe-900 catalyst. Moreover, the selected area electron diffraction (SAED) without any diffraction spots could be observed in Fig. 1f, which confirms that there is no crystal structure related to Fe nanoparticles in PDA-Fe-900. The energy-dispersive spectroscopy (EDS) mappings demonstrate that the N and high-density Fe elements are uniformly distributed on the carbon support (Fig. 1g and Fig. S3 in Supporting information) [34,40,41]. According to inductively coupled plasma mass spectrometry (ICP-MS), the Fe loading of PDA-Fe-900 catalyst is 2.87 wt% higher than that of PD-Fe-900 (2.00 wt%) and DA-Fe-900 (2.50 wt%), which may be due to the synergistic coordination of Phen and DAP with Fe^{2+}.

In wide-angle XRD patterns, similar to the pure N-doped ordered mesoporous carbon catalyst, PDA-Fe-900 only displays two diffraction peaks centered at 23.7° and 43.2° (Fig. 2a). There is no additional diffraction peaks of Fe-based particles (such as metallic iron or other iron compounds) presented in the PDA-Fe-900, which is in line with the SAED and HR-TEM images. By contrast, the XRD patterns of the DA-Fe-900 and PA-Fe-900 catalysts display the diffraction peak of Fe nanoparticles, indicating that DAP and Phen play an essential roles in preventing the agglomeration of metal iron species [42,43]. Also, the PDA-Fe-900 catalyst displays a relatively low degree of graphitization and abundant disordered and amorphous structure, which is further evidenced by Raman spectra [44]. As shown in Fig. 2b, the characteristic disordered carbon (D bands) and sp^2-hybridized graphitic carbon (G bands) at about 1337.8 and 1585.3 cm^{-1}, respectively, and the intensity ratios of D to G band (I_D/I_G) of PDA-Fe-900, PA-Fe-900, DA-Fe-900, and PDA-900 are calculated to be 1.23, 1.14, 1.23 and 1.38, respectively. This reveals a high level of defects in the PDA-Fe-900, which is beneficial to providing more active sites in the ORR process.

N_2 adsorption-desorption isotherms are obtained to evaluate the textural properties of the prepared catalysts and the results are summarized in Table S1 (Supporting information). Apparently, the introduction of SBA-15 provides a significant affect in surface area and mesoporous of the catalyst, as evidenced by the type-IV isotherms with a pronounced H1 hysteresis loop in a relative pressure range from 0.4 to 0.8 (Fig. 2c). PDA-Fe-900 possesses a high BET specific surface area of 1115.0 m^2/g (Table S1 in Supporting information), superior to DA-Fe-900 (941.0 m^2/g), PA-Fe-900 (1083.0 m^2/g), and PDA-900 (820.0 m^2/g), whereas PD-Fe-900 prepared in the absence of SBA-15 templates shows a low BET specific surface area of only 40.0 m^2/g. For the catalysts with SBA-15 templates, the difference of specific surface area is due to the difference in specific components added in the preparation process. It is generally recognized that the large specific surface area of the catalysts is conducive to the exposure of active sites in the electrochemical reactions, thus enhancing the catalytic activity [45,46]. The density functional theory (DFT) pore size distribution curves, represented in Fig. 2d, indicates that the PDA-Fe-900 catalyst primarily contain mesopores with diameters of about 5 nm, further confirming the well-defined ordered mesoporous structure. As reported, mesoporous structure is beneficial to the mass transfer, thus improving ORR catalytic activity. The chemical bonds and functional species of the prepared catalysts have been investigated by FT-IR spectra as shown in Fig. S4a (Supporting information). The bonds corresponding to C−H stretching vibration are centered at approximately 2918 and 1438 cm^{-1}, respectively. The peaks located at 3438, 1629, 1576, 1084 and 1048 cm^{-1} are ascribed to the −OH/−NH, C=O, C=N, C−O/C−N and C−O−C vibrations, respectively. These results reveal that nitrogen/oxygen species have been successfully incorporated into the carbon matrix, which are conducive to enhance the contact performance between the cathode materials and electrolytes, thus accelerating the ion diffusion from solution towards electrode surface. In addition, with the doping of metal Fe, the catalytic material of PDA-Fe-900 shows an obvious Fe-N vibrational absorption peak at 881 cm^{-1}, which is conducive to achieving prominent ORR performance [47].

XPS is performed to analyze the surface elemental compositions and electronic structures of catalysts. Fig. 2e and Table S1 (Supporting information) show that C, N and O are present in PDA-900, while C, N, O, and Fe are observed for PDA-Fe-900, PD-Fe-900, and DA-Fe-900. The content of Fe in PDA-Fe-900, DA-Fe-900, and PA-Fe-900 estimated by XPS is ~2.77 wt%, ~1.95 wt% and ~1.46 wt%, respectively (Table S1 in Supporting information). However, the weight percentages of Fe in the PDA-Fe-900, DA-Fe-900, and PA-Fe-900 based on ICP-MS are 2.87 wt%, 2.50 wt% and 2.00 wt%, re-

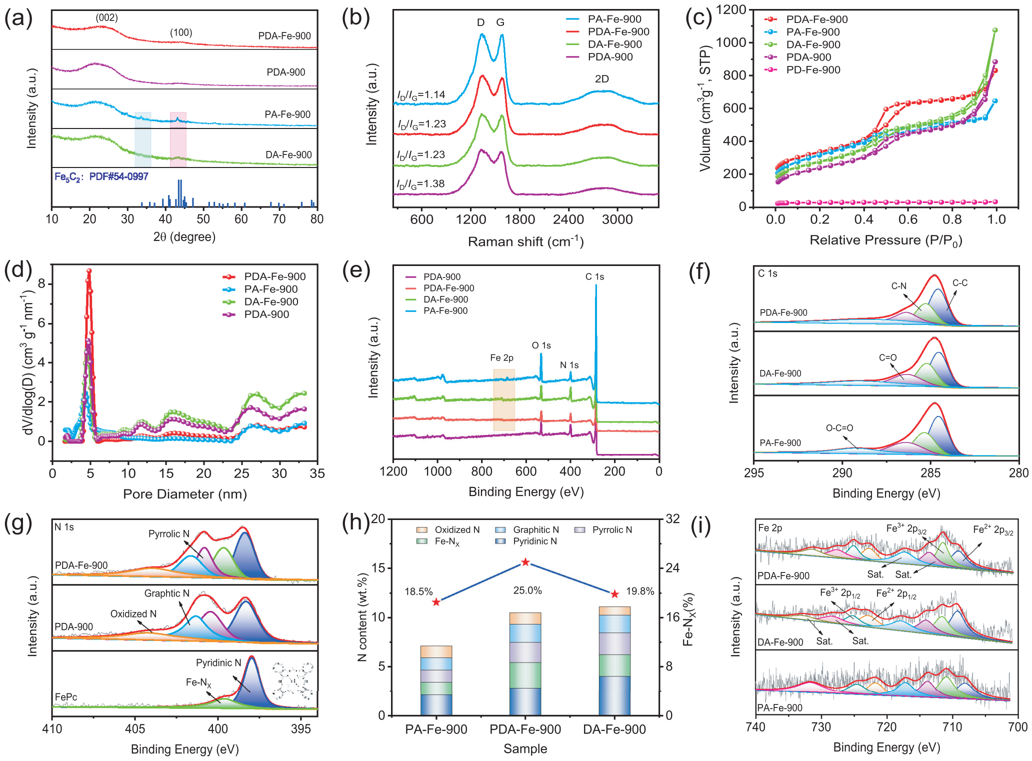

Fig. 2. (a) Wide-angle XRD patterns and (b) Raman spectra of PDA-Fe-900, PA-Fe-900, DA-Fe-900 and PDA-900. (c) N_2 adsorption-desorption isotherms and (d) pore size distribution of PDA-Fe-900, PA-Fe-900, DA-Fe-900, PDA-900 and PD-Fe-900. (e) XPS full spectrum and (f) C 1s of PDA-Fe-900, PA-Fe-900, DA-Fe-900 and PDA-900. (g) N 1s XPS spectra of PDA-Fe-900, FePc and PDA-900. (h) Content of the total N and different N species, the percentage of Fe-N_X and (i) Fe 2p for PDA-Fe-900, PA-Fe-900 and DA-Fe-900.

spectively (Table S1 in Supporting information). The metal Fe content of DA-Fe-900 and PA-Fe-900 from XPS is far below the weight percentage measured by ICP-MS. This difference well demonstrates that the Fe nanoparticles in the DA-Fe-900 and PA-Fe-900 are embedded in the carbon matrix. Additionally, the weight percentage of Fe in the PDA-Fe-900 measured by XPS is consistent with the Fe content measured by ICP-MS, demonstrating that there is no Fe nanoparticle on the carbon matrix of PDA-Fe-900. The high-resolution C 1s spectra show four peaks (Fig. 2f), which are concentrated around 284.6 eV (C–C), 285.3 eV (C–N), 286.4 eV (C–O), and 288.5 eV (O–C=O), respectively [48,49]. The successful N doping into the carbon matrix is confirmed by the appearance of a typical C–N peak in C 1s spectra, which not only serves as anchoring sites for metal atoms, but also tailors the charge/spin density of adjacent carbon atoms to generate active sites for oxygen electrocatalysis. At the same time, the O 1s spectra exhibit four peaks at binding energies of 531.2, 532.6, 533.6 and 536.8 eV, corresponding to –C=O, –C–OH, –C–O–C and –COOH bonds, respectively (Fig. S4b in Supporting information). Oxygen species are profitable for enhancing the contact among the three phases of electrolyte, reactant, and electrode [50].

The fine-scan N 1s spectra for PDA-Fe-900 can be deconvoluted into five different characteristic peaks at about 398.4, 399.6, 400.9, 401.7 and 404.5 eV, corresponding to pyridinic N, Fe-N_X, pyrrolic N, graphitic N, and oxidized N, respectively (Fig. 2g). Compared with PDA-900, the peak value of PDA-Fe-900 at 399.6 eV indicates that Fe has been successfully doped into the carbon matrix and bonded with N. Meanwhile, the peak at 399.6 eV indicates the presence of N in the chemical state similar to Fe-N_X moiety in Phthalocyanine iron (FePc) [42,51]. As well known, Fe-N_X provides highly active oxygen binding sites in the process of ORR kinetics and directly reduces O_2 to H_2O through 4e$^-$-path. It is reported that the relative content of doped N species is an important index of ORR performance than N content [52]. Therefore, the relative content of Fe-N_X is analyzed by calculating the ratio of the Fe-N_X peak area to the total area, displayed in Fig. 2h. The relative content of Fe-N_X of PDA-Fe-900 is 25.0%, higher than that of PA-Fe-900 (18.5%) and DA-Fe-900 (19.8%). The high-density Fe-N_X active sites in PDA-Fe-900 catalyst are attributed due to the formation of numerous Fe-N bonds during the mixing process of Phen and DAP precursors with Fe^{2+}. Elemental analysis demonstrates that N content in the PDA-Fe-900 catalyst reaches up to 10.51 wt% (Table S1 in Supporting information and Fig. 2i), which is the main reason for the high Fe loading of 2.77 wt%. For the Fe 2p spectra in Fig. 2i, two main peaks centered at ∼711.0 and ∼726.0 eV are observed for PDA-Fe-900 sample, which are associated with Fe $2p_{3/2}$ and Fe $2p_{1/2}$, respectively. Through the analysis of Fe 2p spectra, the four peaks located at approximately 709.1, 711.5, 722.7 and 725.1 eV correspond to Fe^{2+} $2p_{3/2}$, Fe^{3+} $2p_{3/2}$, Fe^{2+} $2p_{1/2}$ and Fe^{3+} $2p_{1/2}$, respectively, indicating that Fe ions are the main existing form on the surface of catalytic materials. The Fe^{2+} species on the Fe $2p_{3/2}$ orbital are considered to symbolize the formation of Fe-N_X active sites, which further confirm the existence of Fe-N_X species in the PDA-Fe-900 catalyst [28]. In addition, the satellite peaks are observed at the binding energies of 713.6, 727.6, 717.3 and 731.3 eV, respectively. These results fully demonstrate that the elements of Fe and N are successfully incorporated into the carbon matrix, and Fe coordinates with N to construct Fe-N_X active sites.

The electrochemical performance of PDA-Fe-T catalysts for ORR in alkaline electrolyte is measured by CV curves (Fig. S5 in Supporting information). The results exhibit that the obtained PDA-Fe-900 has the most positive ORR peak potential, indicat-

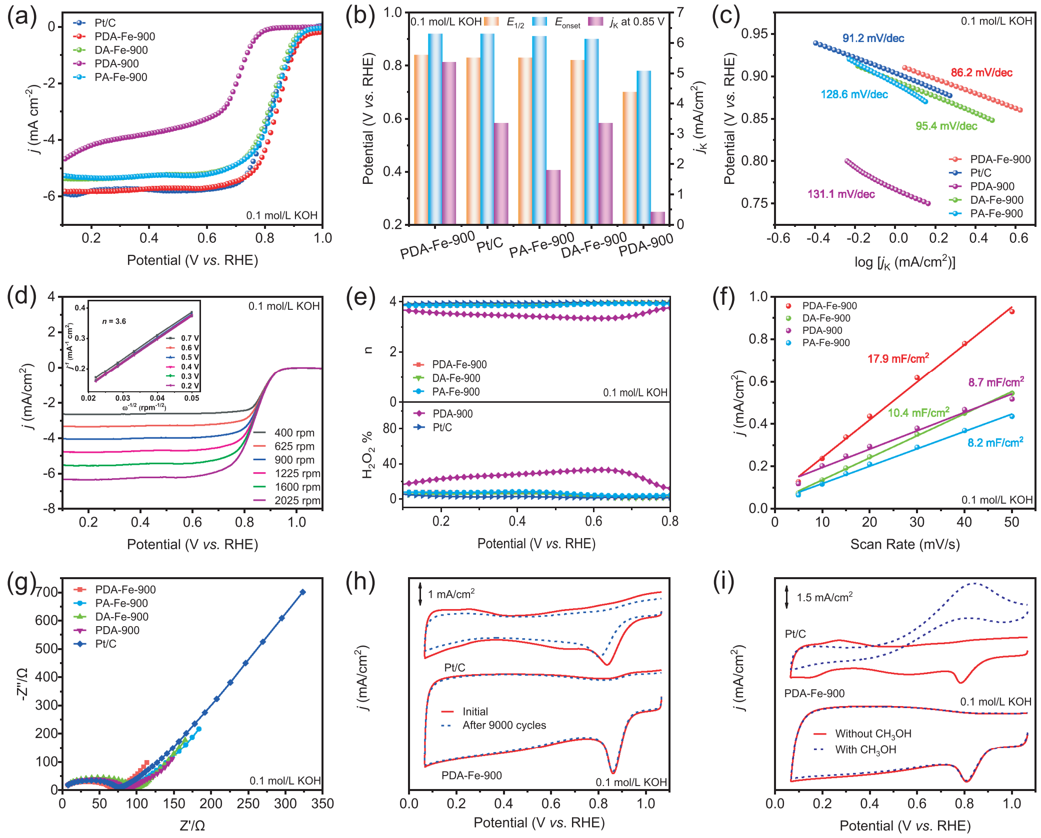

Fig. 3. ORR performance in 0.1 mol/L KOH: (a) LSV curves, (b) j_K, $E_{1/2}$ and E_{onset} and (c) Tafel plots of the PDA-Fe-900, PA-Fe-900, DA-Fe-900, PDA-900 and commercial Pt/C. (d) LSV curves of PDA-Fe-900 at different rotation speeds (inset shows K-L plots at different potentials). (e) n and H_2O_2%. (f) C_{dl}. (g) EIS for the PDA-Fe-900, PA-Fe-900, DA-Fe-900, PDA-900 and commercial Pt/C. (h) CV curves before and after 9000 potential cycles, (i) CV curves before and after addition of CH_3OH solution for PDA-Fe-900 and commercial Pt/C.

ing that 900 °C is the best calcination temperature for the prepared samples. Therefore, 900 °C was chosen as the optimal temperature for experimental exploration. The ORR catalytic activity of PDA-Fe-900, DA-Fe-900, PA-Fe-900 and PDA-900 is evaluated and compared with commercial Pt/C catalyst through CV and LSV in N_2/O_2-saturated 0.1 mol/L KOH. Fig. S6 (Supporting information) shows that CV curves have no cathodic ORR peaks in the N_2-saturated 0.1 mol/L KOH electrolyte. Nevertheless, when the solution is saturated with O_2, all catalysts show well-defined cathodic peaks, implying an evident ORR process. The position of ORR peak shows a significant positive shift for PDA-Fe-900 (0.86 V), in comparison with Pt/C (0.84 V), PDA-900 (0.74 V), DA-Fe-900 (0.84 V), and PA-Fe-900 (0.85 V) samples, demonstrating the preferential ORR reactivity of PDA-Fe-900. To further evaluate the ORR electrocatalytic activity and kinetics of PDA-Fe-900 and comparison samples, the RRDE technique is used to record the LSV curves at 1600 rpm in O_2-saturated 0.1 mol/L KOH solution (Fig. 3a and Table S2 in Supporting information). The PD-Fe-900 with low mesoporous structure exhibited poor electrocatalytic activity ($E_{1/2} = 0.65$ V, $E_{onset} = 0.90$ V) in Fig. S7 (Supporting information). The PDA-900 ($E_{1/2} = 0.70$ V, $E_{onset} = 0.78$ V), DA-Fe-900 ($E_{1/2} = 0.82$ V, $E_{onset} = 0.90$ V), and DA-Fe-900 ($E_{1/2} = 0.83$ V, $E_{onset} = 0.91$ V) also exhibit poor electrocatalytic activity, which is attributed to the low density of Fe-N_X active sites in carbon matrix. Particularly, the PDA-Fe-900 catalyst with high-density Fe-N_X and ordered mesoporous structure displays substantial improvement in ORR activity, as reflected by the shift of $E_{1/2}$ to 0.84 V and E_{onset} to 0.92 V, which is comparable to the corresponding values of commercial Pt/C ($E_{1/2} = 0.83$ V, $E_{onset} = 0.92$ V) (Fig. 3b). Meanwhile, the kinetic current density (j_K) of PDA-Fe-900 at 0.85 V can reach a value 5.36 mA/cm^2, higher than those of Pt/C (3.35 mA/cm^2), PDA-900 (0.42 mA/cm^2), PA-Fe-900 (1.80 mA/cm^2), and DA-Fe-900 (3.35 mA/cm^2).

Moreover, the Tafel slope is employed to evaluate the ORR kinetics of all samples. As disclosed by Fig. 3c, the PDA-Fe-900 catalyst possesses a smaller Tafel slope of 86.2 mV/dec compared with those of Pt/C (91.2 mV/dec), PA-Fe-900 (128.6 mV/dec), DA-Fe-900 (95.4 mV/dec) and PDA-900 (131.1 mV/dec), evidencing a superior ORR reaction kinetics. These results reveal that PDA-Fe-900 has excellent ORR activity, which can be attributed to the dense Fe-N_X sites, rich ordered mesoporous structure, and high specific surface area. The RDE measurement at various rotating rates is performed to further understand the ORR kinetics of catalysts (Fig. 3d). The corresponding K-L plots presented in the inset of Fig. 3d are all nearly linear, confirming the first-order reaction kinetics in 0.1 mol/L KOH solution. According to K-L equation, the n of PDA-Fe-900 is calculated to approach 3.6 over the potential range from 0.1 to 0.8 V, revealing a direct four-electron ORR transfer path, which is also confirmed by the RRDE tests. Fig. 3e shows the n value for PDA-Fe-900 is 3.9, which is comparable to that of Pt/C ($n = 4.0$), further verifying the four-electron ORR path. Moreover, the H_2O_2 yield of PDA-Fe-900 is remained less than 10% in 0.1~0.8 V, resulting in a high-efficiently catalytic selectivity of the oxygen reduction toward H_2O. The C_{dl} can effectively reflect the ECSA of as-prepared catalysts. PDA-Fe-900 catalyst has a C_{dl} value of 17.9 mF/cm^2, which is higher than those PDA-900 (8.7 mF/cm^2), PA-Fe-900 (8.2 mF/cm^2), and DA-Fe-900 (10.4 mF/cm^2), indicating more active sites achieved for PDA-Fe-900 (Fig. 3f and Fig. S8

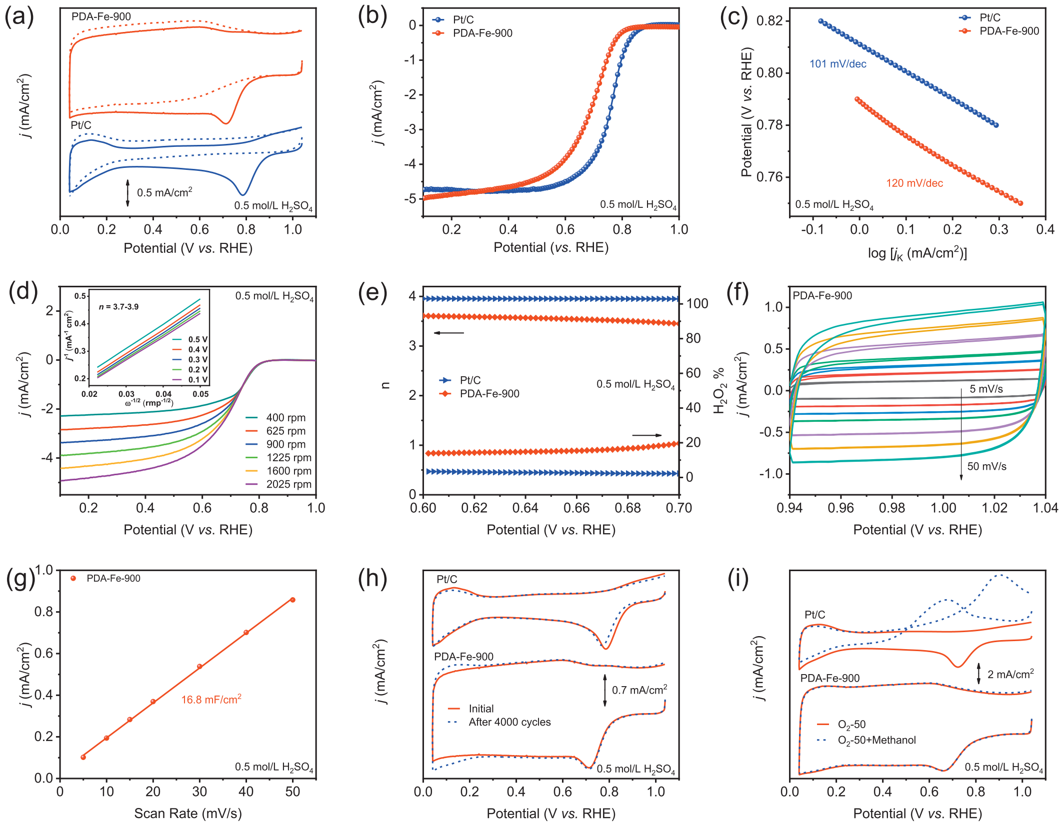

Fig. 4. ORR performances in 0.5 mol/L H_2SO_4: (a) CV curves, (b) LSV curves and (c) Tafel plots of PDA-Fe-900 and commercial Pt/C catalyst. (d) LSV curves of PDA-Fe-900 at different rotating speeds of 400~2025 rpm (inset showing the K-L plots at different potentials). (e) n and H_2O_2%. (f) CV curves of PDA-Fe-900 in 0.5 mol/L H_2SO_4 at different scan rates. (g) C_{dl} of PDA-Fe-900. (h) CV curves before and after 9000 potential cycles. (i) CV curves before and after addition of CH_3OH solution for PDA-Fe-900 and commercial Pt/C.

in Supporting information). The EIS tests are performed to further evaluate the electrochemical properties of the samples (Fig. 3g). Fig. S9 (Supporting information) shows the Nyquist plot of EIS for PDA-Fe-900, including equivalent series resistance (R_s), charge transfer resistance (R_{ct}) and diffusion resistance (R_p), and illustrates the corresponding equivalent circuit diagram. The values of R_s, R_{ct} and R_p for PDA-Fe-900 are 1.26, 63.22 and 0.32 Ω, which are lower than 2.88, 63.97 and 0.33 Ω of Pt/C, indicating that PDA-Fe-900 has low impedance and fast charge transfer rate. In addition, the PDA-Fe-900 also exhibits a superior long-term stability and methanol crossover tolerance. After 9000 cycles of CV at a scan rate of 50 mV/s within the potential range of 0-1.1 V in 0.1 mol/L KOH solution, the peak potential of PDA-Fe-900 hardly changes, meanwhile the commercial Pt/C shows an obvious attenuation of 20 mV in Fig. 3h. Above results confirm the strong electrochemical stability of PDA-Fe-900, which could be ascribed to the unique N-doped ordered mesoporous carbon as substance to anchor the Fe species with high chemical stability. The CV curves for ORR upon the immediate addition of methanol are also measured at 50 mV/s. As shown in Fig. 3i, after the addition of 1 mL methanol solution into the electrolyte, the oxygen reduction peak of Pt/C sharply vanishes and appears an obvious oxidation peak, whereas the oxygen reduction peak changes are negligible for PDA-Fe-900, demonstrating the superior methanol resistance [53,54]. These experimental results suggest that PDA-Fe-900 has excellent four-electron ORR selectivity, methanol crossover effects and excellent long-term cycling stability.

The ORR electrocatalytic activity of PDA-Fe-900 is also assessed by CV and LSV measurements in 0.5 mol/L H_2SO_4 solution. The commercial Pt/C is also tested in the same conditions for comparison. The CV curve of PDA-Fe-900 shows an obvious peak at 0.75 V, demonstrating an optimistic ORR catalytic activity (Fig. 4a). The LSV test is performed using RRDE to further evaluate the electrocatalytic activity of as-prepared samples. As shown Fig. 4b, PDA-Fe-900 displays a good ORR activity with the E_{onset} of 0.78 V and $E_{1/2}$ of 0.70 V, which are close to the benchmark Pt/C ($E_{onset} = 0.82$ V, $E_{1/2} = 0.76$ V) and most of reported non-noble metal ORR catalysts (Table S4 in Supporting information). The Tafel slope of PDA-Fe-900 (120 mV/dec) is similar that of Pt/C (101 mV/dec), which further confirms the high-efficiency ORR activity and faster ORR kinetic (Fig. 4c). The K-L plots of PDA-Fe-900 is obtained from the polarization curves at different rotation rates measured by RDE tests, which present good linearity and parallelism at different potentials. The calculated n for PDA-Fe-900 is about 3.7-3.9 by the K-L equation over the potential range of 0.1-0.5 V, which is compatible to the value of 4 for commercial Pt/C (Fig. 4d). In addition, RRDE measurements further evaluate the n (~3.6) and H_2O_2 yield (remains below 20%), indicating that the direct four-electron ORR catalytic path on the PDA-Fe-900 catalyst (Fig. 4e). In addition, PDA-Fe-900 exhibits a C_{dl} of 16.8 mF/cm^2, implying that the PDA-Fe-900 possesses a larger ECSA, and more active sites are exposed (Figs. 4f and g). Long-term cycle stability and methanol tolerance are also important parameters to evaluate the ORR performance of electrocatalysts. The durability of the PDA-Fe-900 catalyst as shown in Fig. 4h, and no obvious decay in the reduction peak potential is detected after 4000 cycles, demonstrating the superior stability of PDA-Fe-900. Furthermore, PDA-Fe-900 possess an excellent methanol tolerance compared to Pt/C (Fig. 4i). In short, PDA-Fe-900 delivers an excellent ORR performance with enhanced kinetics and catalytic activity comparable to that of commercial

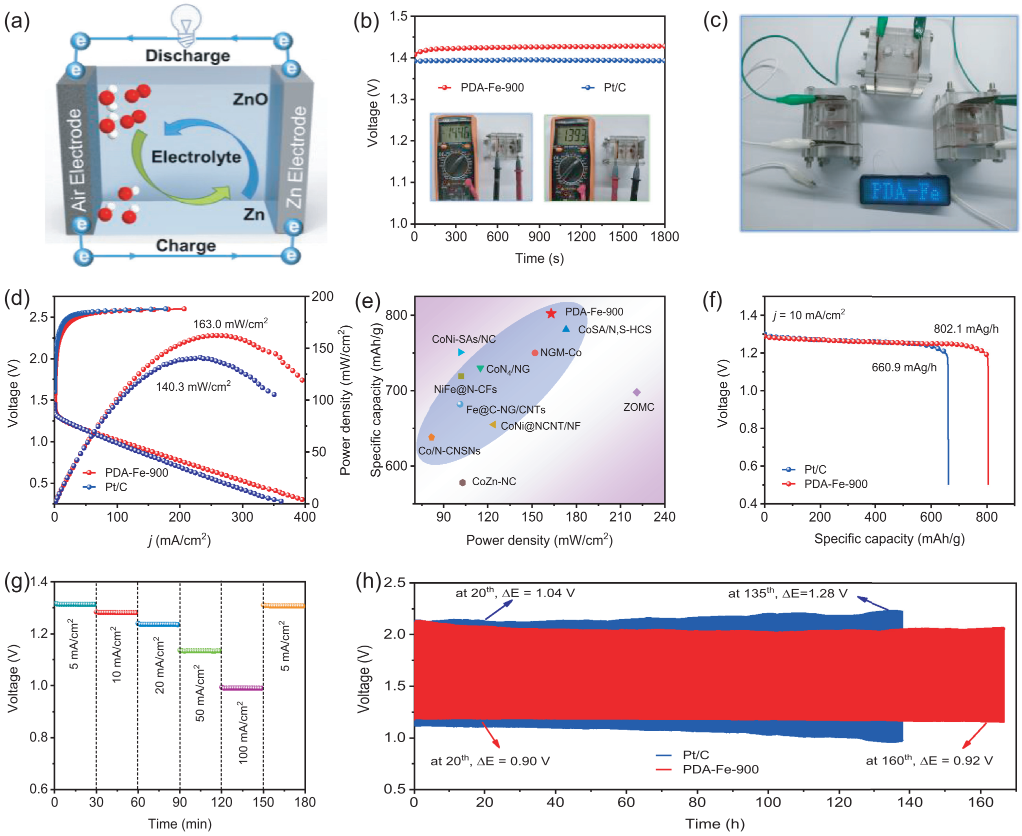

Fig. 5. Liquid rechargeable ZAB: (a) Schematic configuration of liquid rechargeable ZAB. (b) OCV of ZABs based on PDA-Fe-900 and Pt/C. (c) Power supply of LED screen by three series-connected PDA-Fe-900 based ZABs. (d) Polarization and power density curves of the ZAB using PDA-Fe-900 and Pt/C. (e) Comparison of the power density and specific capacity for PDA-Fe-900 and the recently reported catalysts in supplementary Table S5 in Supporting information. (f) Discharge curves at a current density of 10 mA/cm^2. (g) Discharge curves of the PDA-Fe-900 based ZABs at various current densities (5-100 mA/cm^2). (h) Stability at a content current density of 5 mA/cm^2.

Pt/C in alkaline and acidic electrolytes, which is attributed to the dense and accessible Fe-N$_X$ sits. In addition, the ordered mesoporous structures play essential roles in ORR performance, in the following aspects: (1) Ordered mesoporous materials with uniform pore size distribution and long-range ordered pore channels ensure the rapid transport of reactants and products (OOH*, OH*, OH$^-$, H_2O, *etc.*) in the ORR process, thus increasing the catalytic activity. (2) The three-dimensional interconnected pores of the ordered mesoporous carbon skeleton enhance the accessibility of Fe-N$_X$ sites, which is of significance for improving the half-wave potential of ORR. (3) The orderly interconnected graphitized framework has excellent thermal stability and effectively avoids the collapse of pore structures, which can improve the structural stability of the catalytic materials.

For rechargeable ZAB cathode, ORR and OER take place during the discharging and charging process, respectively. It is necessary to require ORR/OER bifunctional electrocatalysts as air electrode for ZABs. The OER performance of PDA-Fe-900, IrO_2, and Pt/C were assessed by employing LSV determination at 1600 rpm in 1 mol/L KOH electrolyte. As shown in Fig. S9 (Supporting information), the Pt/C catalyst exhibits the worst OER activity in contrary to its excellent ORR activity. Generally, the overpotential at 10 mA/cm^2 is usually utilized for assessing the activity of OER. PDA-Fe-900 provides an OER overpotential of 0.44 V at a current density of 10 mA/cm^2, which is slightly lower than that of IrO_2 (0.34 V). The bifunctional activity of PDA-Fe-900 is expected to show a better discharging/charging performance for rechargeable ZABs. As shown in Fig. 5a, a liquid rechargeable ZAB is assembled by using PDA-Fe-900 loaded carbon paper as the air cathode, Zn plate as the anode and 6.0 mol/L KOH containing 0.2 mol/L $Zn(OAc)_2$ as the electrolyte. For comparison, the rechargeable ZAB using commercial Pt/C as air cathode is also assembled and tested under the identical conditions. The ZAB based on PDA-Fe-900 affords an open-circuit voltage (OCV) of 1.44 V (Fig. 5b), which is higher than 1.39 V for commercial Pt/C based ZAB. Also, three PDA-Fe-900 based ZABs in series can illuminate a light-emitting diode screen (LED, 4.5 V), demonstrating the great potential for powering practical energy electronics equipment (Fig. 5c). The charge-discharge polarization curves are illustrated in Fig. 5d, a much higher discharge current density and a slightly lower charge voltage gap are obtained on PDA-Fe-90 base ZAB compared to that of Pt/C based ZAB, manifesting the superior activity and excellent rechargeable capability of PDA-Fe-900 based ZAB. Moreover, the ZAB based on PDA-Fe-900 catalyst delivers a large peak power density of 163.0 mW/cm^2 (Fig. 5d), higher than that of the commercial Pt/C based ZAB (140.3 mW/cm^2) and other reported non-noble catalysts (Fig. 5e and Table S5 in Supporting information).

Additionally, Fig. 5f shows the galvanostatic discharge curves of PDA-Fe-900 and Pt/C driven ZABs at a constant current density of 10 mA/cm^2. By normalizing with respect to the mass of consumed Zn, the specific capacity of PDA-Fe-900 based ZAB is calculated to be 802.1 mAh/g, superior to that of Pt/C based ZAB (660.9 mAh/g) as well as ZABs based on recently reported catalysts (Fig. 5e and Table S5 in Supporting information) [55]. The galvanostatic discharge curves of PDA-Fe-900 driven ZAB at different current densities from 5 to 100 mA/cm^2 exhibit the stable potential plateaus, which confirms the excellent rate performance of PDA-Fe-900 driven ZAB (Fig. 5g). In addition, the long-term cycle stability

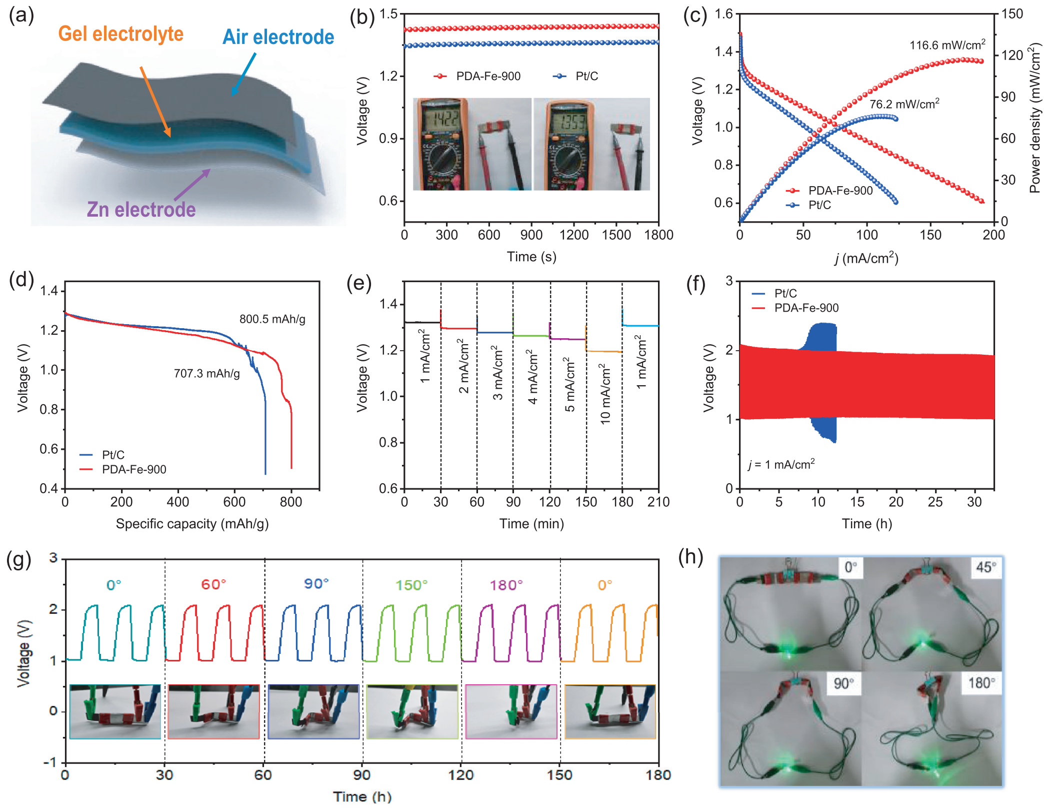

Fig. 6. Flexibility rechargeable ZAB: (a) Schematic illustration of flexibility rechargeable ZAB. (b) OCV of ZABs based on PDA-Fe-900 and Pt/C. (c) Discharge polarization curves and corresponding power densities of ZABs based on PDA-Fe-900 and Pt/C. (d) Discharge curves at a current density of 5 mA/cm^2. (e) Discharge curves of the PDA-Fe-900-based ZABs at various current densities. (f) Galvanostatic charge/discharge cycling performance of ZAB based on PDA-Fe-900 and Pt/C at a current density of 1 mA/cm^2. (g) Cycling stability of the ZAB under different bending angles. (h) Photographs of a LED light powered by two flexible ZAB based on PDA-Fe-900 under different bending deformations.

of liquid rechargeable ZAB with PDA-Fe-900 is further evaluated by continuous galvanostatic discharge-charge test at 5 mA/cm^2 with 10 min per cycle (Fig. 5h). Obviously, the PDA-Fe-900 based ZAB can stably operate for a longer time than Pt/C based ZAB. Specifically, the PDA-Fe-900 based ZAB delivers an excellent stability over 160 h, and the charge-discharge voltage range shows only a slight increase from 0.90 V in 20th h to 0.92 V at 160th h. On the contrary, the Pt/C based ZAB exhibits the poor cycle life of 135 h, and the charge-discharge voltage range changes significantly from the 1.04 V in 20th h to 1.28 V at 135th h. These results reveal that the PDA-Fe-900 based ZAB displays an unprecedented rechargeable ability and long-term stability. As well known, the ZABs performance is mainly related to the porous structure of the cathode catalysts. Therefore, this unique ordered mesoporous structure accompanying with abundant accessible Fe-N$_X$ active sites endows PDA-Fe-900 catalyst a promising Pt/C catalyst alternative to achieve the long-term stability of ZABs.

Inspired by the increasing demand for flexible energy storage devices, flexible solid-state ZABs are assembled with PDA-Fe-900 as air cathode, alkaline polyacrylic acid gel as the electrolyte, and Zn plate as the anode (Fig. 6a). In Fig. 6b, the OCV of flexible solid-state ZABs based on PDA-Fe-900 and commercial Pt/C is 1.42 V and 1.35 V, respectively, indicating that PDA-Fe-900 based flexible solid-state ZAB has better performance. As shown in Fig. 6c, the flexible solid-state ZAB with PDA-Fe-900 delivers a maximum power density of 119.0 mW/cm^2, exceeding the ZAB with Pt/C (90.0 mW/cm^2) and most of recently reported non-noble catalysts (Table S6 in Supporting information). The PDA-Fe-900 also endows the flexible solid-state ZAB with a higher specific capacity of 800.5 mAh/g than Pt/C (707.3 mAh/g) at current density of 5 mA/cm^2 based on consumed Zn weight (Fig. 6d). Fig. 6e shows the stable voltage plateaus of PDA-Fe-900 based all-solid-state ZAB at various current densities (1∼5 mA/cm^2). And the discharging voltage of PDA-Fe-900 based flexible solid-state ZAB can be well-recovered to around 1.32 V when the current density is restored to 1 mA/cm^2, suggesting the good rate performance and stability of PDA-Fe-900 based flexible solid-state ZAB. To further examine the stability and reversibility of the ZAB, chronopotentiometry test is performed at a current density of 1 mA/cm^2 with 10 min per cycle. As depicted in Fig. 6f, the flexible solid-state ZAB based on PDA-Fe-900 yields an initial discharge voltage of 1.00 V and charge voltage of 2.05 V (voltage gap of 1.05 V), and only a slight voltage change is discerned over 30 h. In contrast, the performance of the Pt/C air cathode is severely deteriorative with the voltage gap increasing after 10 h. This result shows PDA-Fe-900 catalyst possesses excellent durability in flexible solid-state ZAB. Moreover, the device can be bent to different angle (0∼180°) without obvious charge-discharge potential changes, indicating the excellent mechanical flexibility and stability of the PDA-Fe-900 based flexible ZAB in Fig. 6g. As a demonstration, a LED light (2.5 V) can be powered using two flexible solid-state ZABs connected in series even under bending conditions (Fig. 6h). These results manifest the application prospects of PDA-Fe-900 catalyst based flexible solid-state ZAB for flexible electronic devices in the future.

In summary, the Fe, N co-doped ordered mesoporous carbon fiber bundles have been designed as efficient ORR electrocatalyst. The optimized PDA-Fe-900 catalyst exhibits excellent catalytic activity and stability in both alkaline and acidic conditions, ascribed to the following two reasons: firstly, the high-density Fe-N$_X$ sites exist uniformly in the carbon fibers as activity centers, which help to improve the adsorption of ORR intermediates; secondly, the ordered mesoporous structure of catalyst facilitates the mass transfer during the electrocatalytic process, and the high specific surface area is beneficial to the exposure of Fe-N_X sites. When used as the catalyst for cathodic ORR in ZAB, PDA-Fe-900 electrode exhibits a higher power density of 163.0 mW/cm^2 and better cycling stability (over 160 h) than those of Pt/C-based ZAB. Further, the assembled flexible solid-state ZAB exhibits distinct flexibility and stable performance under bending and compressing conditions. These experimental results reveal the significance of optimizing mass transport capability and improving the density of Fe-N_X sites for ORR catalyst. This work provides a feasible route for synthesizing non-precious metal catalysts for ZABs applications.

Declaration of competing interest

The authors declare that they have no known competing financial interests or personal relationships that could have appeared to influence the work reported in this paper.

Acknowledgments

This work was supported by the National Natural Science Foundation of China (No. U1804255), and the Key Research & Development and Promotion Projects in Henan Province (Nos. 222102520038 and 212102210651).

Supplementary materials

Supplementary material associated with this article can be found, in the online version, at doi:10.1016/j.cclet.2023.108142.

References

[1] M.K. Debe, Nature 486 (2012) 43–51.
[2] Z.P. Cano, D. Banham, S. Ye, et al., Nat. Energy 3 (2018) 279–289.
[3] H. Wang, L. Cao, Y. Feng, et al., Chin. Chem. Lett. 34 (2023) 107601.
[4] Y. Zhao, Y. Liu, Z. Zhang, et al., Nano Energy 97 (2022) 107124.
[5] H. Sun, M. Zhao, C. Ma, et al., Nano Res. 16 (2023) 4980–4986.
[6] Y.P. Deng, Y. Jiang, R. Liang, et al., Nat. Commun. 11 (2020) 1952.
[7] H. Zhang, M. Zhao, H. Liu, et al., Nano Lett. 21 (2021) 2255–2264.
[8] M. Zhao, H. Liu, H. Zhang, et al., Energy Environ. Sci. 14 (2021) 6455–6463.
[9] J.N. Liu, C.X. Zhao, D. Ren, et al., Adv. Mater. 34 (2022) 2109407.
[10] M. Xiao, Z. Xing, Z. Jin, et al., Adv. Mater. 32 (2020) 2004900.
[11] Z.W. Seh, J. Kibsgaard, C.F. Dickens, et al., Science 355 (2017) 4998.
[12] J. Zhu, M. Xiao, Y. Zhang, et al., ACS Catal. 6 (2016) 6335–6342.
[13] J. Wang, W. Liu, G. Luo, et al., Energy Environ. Sci. 11 (2018) 3375–3379.
[14] C.X. Zhao, B.Q. Li, J.N. Liu, et al., Chin. Chem. Lett. 30 (2019) 911–914.
[15] Z. Li, L. Leng, S. Ji, et al., J. Energy Chem. 73 (2022) 469–477.
[16] X. Xie, C. He, B. Li, et al., Nat. Catal. 3 (2020) 1044–1054.
[17] C. Tang, Y. Jiao, B. Shi, et al., Angew. Chem. Int. Ed. 59 (2020) 9171–9176.
[18] M. Zhang, B. Yang, T. Yang, et al., Chin. Chem. Lett. 33 (2022) 362–367.
[19] L. Peng, J. Yang, Y. Yang, et al., Adv. Mater. 34 (2022) 2202544.
[20] C. Zhang, W. Zhang, W. Zheng, ChemCatChem 11 (2018) 655–668.
[21] J. Yan, K. Zeng, W. Hu, et al., ACS Sustain. Chem. Eng. 10 (2022) 7553–7563.
[22] H. Yang, X. Wang, S. Wang, et al., Carbon 182 (2021) 109–116.
[23] X. Wan, Q. Liu, J. Liu, et al., Nat. Commun. 13 (2022) 2963.
[24] J.C. Li, M. Cheng, T. Li, et al., J. Mater. Chem. A 7 (2019) 14478–14482.
[25] J. Xue, Y. Li, J. Hu, J. Mater. Chem. A 8 (2020) 7145–7157.
[26] Y. Zhan, F. Xie, H. Zhang, et al., ACS Appl. Mater. Interfaces 12 (2020) 17481–17491.
[27] X. Xie, L. Peng, H. Yang, et al., Adv. Mater. 33 (2021) 2101038.
[28] J. Han, X. Meng, L. Lu, et al., Adv. Funct. Mater. 29 (2019) 1808872.
[29] J. Ortiz-Medina, Z. Wang, R. Cruz-Silva, et al., Adv. Mater. 31 (2019) 1805717.
[30] H. Shen, H. Peng, R. Cao, et al., J. Phys. Chem. Lett. 12 (2021) 517–524.
[31] S. Gao, Y. Liu, Z. Xie, et al., Small Methods 5 (2021) 2001039.
[32] H. Shen, E. Gracia-Espino, J. Ma, et al., Nano Energy 35 (2017) 9–16.
[33] C. Zhu, H. Li, S. Fu, et al., Chem. Soc. Rev. 45 (2016) 517–531.
[34] J. Han, H. Bao, J.Q. Wang, et al., Appl. Catal. B 280 (2021) 119411.
[35] G. Chen, P. Liu, Z. Liao, et al., Adv. Mater. 32 (2020) 1907399.
[36] Y. Wu, Y. Yang, T. Gao, et al., Sustain. Energy Fuels 4 (2020) 4117–4125.
[37] C. Zhu, Q. Shi, B.Z. Xu, et al., Adv. Energy Mater. 8 (2018) 1801956.
[38] Y. Zhang, C. Li, Z. Chen, et al., Catal. Lett. 147 (2016) 253–260.
[39] C. Li, Z. Han, Y. Yu, et al., RSC Adv. 6 (2016) 15167–15174.
[40] S. Gao, X. Li, L. Li, et al., Nano Energy 33 (2017) 334–342.
[41] X. Li, B.Y. Guan, S. Gao, et al., Energy Environ. Sci. 12 (2019) 648–655.
[42] L. Zhao, Y. Zhang, L.B. Huang, et al., Nat. Commun. 10 (2019) 1278.
[43] T. Yang, Y. Chen, Y. Liu, et al., Chin. Chem. Lett. 33 (2021) 2171–2177.
[44] Y. Ma, D. Chen, D. Zhang, et al., Carbon 187 (2022) 196–206.
[45] Y. Zhao, X. Li, X. Jia, et al., Nano Energy 58 (2019) 384–391.
[46] Y. Zhao, Y. Liu, Y. Chen, et al., J. Mater. Chem. A 9 (2021) 18251–18259.
[47] M. Sun, D. Davenport, H. Liu, et al., J. Mater. Chem. A 6 (2018) 2527–2539.
[48] F. Zhang, Y. Chen, Y. Liu, et al., Int. J. Hydrog. Energy 46 (2021) 37895–37906.
[49] G. Wei, X. Liu, Z. Zhao, et al., Chem. Eng. J. 455 (2023) 140721.
[50] H. Gong, X. Zheng, K. Zeng, et al., Carbon 174 (2021) 475–483.
[51] G. Wu, C.M. Johnston, N.H. Mack, et al., J. Mater. Chem. 21 (2011) 11392–11405.
[52] T. Yang, S. Fan, Y. Li, et al., Chem. Eng. J. 419 (2021) 129590.
[53] M.S. Thorum, J.M. Hankett, A.A. Gewirth, J. Phys. Chem. Lett. 2 (2011) 295–298.
[54] Y. Chen, S. Ji, S. Zhao, et al., Nat. Commun. 9 (2018) 5422.
[55] F. Kong, X. Fan, A. Kong, et al., Adv. Funct. Mater. 28 (2018) 1803973.